

Searching Ternary Oxides and Chalcogenides as Positive Electrodes for Calcium Batteries

Wang Lu,[†] Juefan Wang,[†] Gopalakrishnan Sai Gautam,^{*,‡} and Pieremanuele Canepa^{*,†,¶}

[†]*Department of Materials Science and Engineering, National University of Singapore, 9 Engineering Drive 1, 117575, Singapore*

[‡]*Department of Materials Engineering, Indian Institute of Science, Bangalore 560012, India*

[¶]*Department of Chemical and Biomolecular Engineering, National University of Singapore, 4 Engineering Drive 4, 117585, Singapore*

E-mail: saigautamg@iisc.ac.in; pcanepa@nus.edu.sg

Abstract

The identification of alternatives to the Lithium-ion battery architecture remains a crucial priority in the diversification of energy storage technologies. Accompanied by the low reduction potential of Ca^{2+}/Ca , -2.87 V vs. SHE, metal-anode-based rechargeable Calcium (Ca) batteries appear competitive in terms of energy densities. However, the development of Ca-batteries lacks high-energy density intercalation cathode materials. Using first-principles methodologies, we screen a large chemical space for potential Ca-based cathode chemistries, with composition of $\text{Ca}_i\text{TM}_j\text{Z}_k$, where TM is a 1st or 2nd row transition metal and Z is oxygen, sulfur, selenium or tellurium. 10 materials are selected and their Ca intercalation properties are investigated. We identify two previously unreported promising electrode compositions: the post-spinel CaV_2O_4 and the

layered CaNb_2O_4 , with Ca migration barriers of ~ 654 meV and ~ 785 meV, respectively. Finally, we analyse the geometrical features of the Ca migration pathways across the 10 materials studied and provide an updated set of design rules for the identification of good ionic conductors, especially with large mobile cations.

1 Introduction

The lithium (Li)-ion battery technology is well-established and has been commercialized for the past three decades, with important but incremental improvements in terms of its energy density, reliability, and safety.¹⁻⁷ However, the energy density prerequisites to drive stationary energy storage devices and electric vehicles are quickly exceeding the limits of what can be achieved by commercial Li-ion batteries.⁸ Finding suitable alternatives to the rocking-chair Li-ion battery is thus a crucial priority in the diversification and modernisation of energy storage technologies. Rechargeable energy-storage devices based on multivalent ions, e.g., magnesium Mg^{2+} , calcium Ca^{2+} , and zinc Zn^{2+} , have emerged as interesting alternatives to their Li-ion analogues.^{9,10} In particular, metal-anode-based rechargeable Ca batteries appear competitive in terms of energy densities, given the high gravimetric capacity, ~ 2205 mAh/g, low standard reduction potential of Ca^{2+}/Ca , -2.87 V vs. SHE, and large volumetric capacity, ~ 2073 Ah/l.⁹⁻¹³

While a Ca-based chemistry is promising in theory, a number of unresolved challenges stand out. First of all, the lack of practical electrolytes that can simultaneously tolerate the reducing environment of a Ca-metal anode and the oxidizing nature of a high-voltage (and high-capacity) Ca-intercalation cathode.¹⁴⁻³¹ Another significant challenge is the identification of fast Ca^{2+} conductors that can act as reversible, high-voltage, and high-capacity intercalation cathodes, which is the focus of this work.³²⁻³⁴

A reasonable figure of merit to identify potential Ca-cathodes with high Ca-conductivity is represented by the migration barrier, E_m —the energy that Ca^{2+} must overcome during its migration between two identical crystallographic sites in an anion host framework. Rong

et al.³² proposed values of $\sim 525\text{--}650$ meV as tolerable limits for E_m in electrodes, where the lower (upper) limit represents micron (nano) sized electrode particles operating at room temperature and a C/2 rate. If the cathode particle sizes are decreased or the temperature of operation is increased or the rate of battery (dis)charge decreased, the upper limit on E_m can be further increased.³³ For example, the upper limit on E_m can be increased up to ~ 895 meV if the cathode particles of size 10 nm are cycled at 333 K (~ 60 °C) at a C/6 rate (6 hours of charge/discharge).³³

Implementing the E_m criteria, Rong et al.³² investigated a number of close-packed frameworks predominantly used in Li-ion batteries, i.e., the spinel (Mn_2O_4), the layered (NiO_2), and the olivine (FePO_4) prototypes, respectively. Three design rules to facilitate the identification of fast multivalent-conductors were discovered, based on the cation coordination environments and the volume per anion available in a host framework (see Sec. 3 for a detailed description).^{32,35} Given the large values (> 525 meV) of E_m estimated for Ca migration in layered and olivine frameworks, and the intrinsic instability of Ca-containing spinel frameworks, the authors concluded that these structures are unsuitable for Ca batteries.³²

Recently, Vaughey and coworkers reported reversible intercalation of 0.6 mol Ca^{2+} into NaSICON- $\text{NaV}_2(\text{PO}_4)_3$, equivalent to a capacity of ~ 81 mAh/g at 3.2 V vs. Ca/Ca^{2+} ,³⁶ while similar experiments with olivine- FePO_4 yielded partially reversible Ca intercalation, with an initial capacity of ~ 72 mAh/g at ~ 2.9 V vs. Ca/Ca^{2+} .³⁶ These experimental results on olivine- FePO_4 are in qualitative agreement with Rong et al.,³² who predicted a moderate Ca migration barrier (~ 580 meV) in the charged state of olivine- FePO_4 . Recently, the group of Kang could reversibly extract Ca^{2+} -ions from $\text{Na}_{1.5}\text{VPO}_{4.8}\text{F}_{0.7}$ and reported a capacity of 87 mAh g^{-1} and 90% capacity retention over 500 cycles.³¹

Additional theoretical work^{32,37} revealed that E_m for Ca in $\delta\text{-V}_2\text{O}_5$ could be as low as ~ 200 meV. However, $\delta\text{-V}_2\text{O}_5$ is not the stable polymorph, with E_m for Ca being predicted to be prohibitively high ($\sim 1700\text{--}1900$ meV) in the stable $\alpha\text{-V}_2\text{O}_5$ polymorph.³⁷ Although Ca intercalation in $\alpha\text{-V}_2\text{O}_5$ has received significant attention,^{38–40} Verrelli et al.³⁹ confirmed the

unsuitability of V_2O_5 as a cathode for Ca batteries owing to lack of robust Ca intercalation, chemically or electrochemically.

Nevertheless, the search for potential Ca cathodes has progressed steadily in the recent past with a handful of research groups fully dedicated to the task. For example, the teams led by Palacín and Ponrouch have extensively investigated TiS_2 using different temperatures, electrolyte formulations, and observed reversible Ca intercalation (accompanied by solvent co-intercalation) from a $Ca(TFSI)_2:PC$ electrolyte at moderate temperatures (~ 60 °C and 100 °C).^{41,42} The same teams have also reported the irreversible Ca extraction from $Ca_{0.89}TaN_2$.⁴³ Tirado and collaborators observed Ca intercalation from a non-aqueous electrolyte into the hydrated phase of layered- α - MoO_3 ,⁴⁴ and claimed a gravimetric capacity of ~ 100 mAh/g at a low voltage of ~ 1.3 V vs. Ca/Ca^{2+} , with additional corroboration from computational models.

On the computational front, using density functional theory (DFT^{45,46}) Arroyo-de Domínguez et al. spearheaded the investigation (and discovery) of alternative Ca-intercalation chemistries, including oxide (i.e., $CaMn_2O_4$, $Ca_2Mn_2O_5$, $CaMn_4O_8$, $Ca_2Fe_2O_5$, $Ca_4Fe_9O_{17}$, $Ca_3Co_4O_9$ and $Ca_3Co_2O_6$) and mixed anion (i.e., $CaFeSO$, $CaCoSO$, $CaNiN$, Ca_3MnN_3 , $Ca_2Fe(Si_2O_7)$, $CaM(P_2O_7)$ with $M=V, Cr, Mn, Fe$ and Co , $CaV_2(P_2O_7)_2$, $Ca(VO)_2(PO_4)_2$, and α - $VOPO_4$) frameworks.⁴⁷⁻⁵² For example, they reported a low Ca E_m of ~ 650 meV in α - $VOPO_4$, along with the high theoretical gravimetric capacity (~ 312 mAh/g) and average (theoretical) intercalation voltage of ~ 2.8 V vs. Ca/Ca^{2+} , making $VOPO_4$ a promising candidate for further experimental investigation.

Undoubtedly, the above experimental and theoretical studies have made sizeable progress towards the development of practical Ca-battery prototypes. However, a more streamlined theoretical (and experimental) effort can accelerate the search for cathodes with facile Ca^{2+} migration, thus facilitating the development of this promising energy storage platform. Here, we have used an efficient screening of Ca-containing ternary structures, utilising a combination of structural information, characterization conditions, and theoretically-predicted

thermodynamic stability, and subsequently evaluated the battery properties of key candidates using DFT-based calculations to push forward the discovery of novel Ca-cathodes. We focus on unveiling overlooked potential cathode chemistries with a general composition of $\text{Ca}_i\text{TM}_j\text{Z}_k$, where TM is a 1st or 2nd row transition metal and Z is oxygen, sulfur or selenium. In the present work, we have not considered any low gravimetric-capacity, mixed anion frameworks or any halogen-based structures.

From our search, we propose two new promising candidates, namely post-spinel CaV_2O_4 and the layered CaNb_2O_4 . Specifically, the calculated E_m in both CaV_2O_4 (~ 654 meV) and CaNb_2O_4 (~ 785 meV) fulfil the criteria for Ca-conductors with reasonable Ca-conductivity. As further validation of our proposed screening strategy, we re-discovered the Chevrel- Mo_6S_8 and CaMoO_3 compounds, which have already been studied both computationally and experimentally.^{44,48,53} Finally, we revisit and propose modifications to the design rules proposed by Rong *et al.* for good multivalent conductors,³² which can be further extended to discover novel conductors for Ca-batteries and beyond.

2 Results

2.1 Screening Procedure of $\text{Ca}_i\text{TM}_j\text{Z}_k$ Electrode Materials

Figure 1a shows the distribution of Ca-containing ternary compounds, with prototype formula $\text{Ca}_i\text{M}_j\text{Z}_k$, where M is a generic cation (and not necessarily an open-shell transition metal) and Z is the anion species, as obtained from the inorganic crystal structure database (ICSD).^{54,55} We excluded structures with non-Ca cations that can potentially exhibit electrochemical activity, such as Li, Na, Mg, Zn, K, Rb, and Cs, from the list of cations considered as M. In the remainder of this study we will address as chalcogenides all compounds with formula $\text{Ca}_i\text{M}_j\text{Z}_k$ where Z can be O, S, Se, or Te. Of the more than 210,000 structures in ICSD, only 412 satisfy the compositional constraint of $\text{Ca}_i\text{M}_j\text{Z}_k$, with Z = O, S, Se, or Te. Furthermore, a significant portion of identified $\text{Ca}_i\text{M}_j\text{Z}_k$ are unsurprisingly oxides^{56,57}

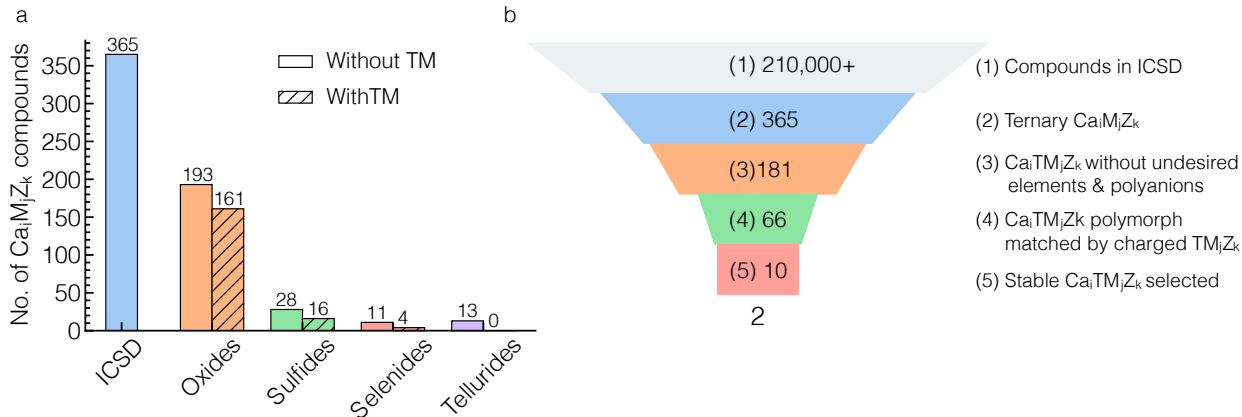


Figure 1: (a) Distribution of ternary $\text{Ca}_i\text{M}_j\text{Z}_k$ compounds, where $\text{Z} = \text{O}, \text{S}, \text{Se},$ or Te and M is a non-Ca cation. Hatched bars indicate $\text{Ca}_i\text{TM}_j\text{Z}_k$ -like compounds with a transition metal (TM) of the d -block and Z any chalcogen element, i.e., $\text{O}, \text{S}, \text{Se}$ or Te . (b) Filtering procedure to identify ternary Ca-containing electrodes with composition of $\text{Ca}_i\text{TM}_j\text{Z}_k$, where TM is redox-active. The number in each coloured panel identifies the number of accepted materials at each stage of the screening.

(orange bars in Figure 1a), with a considerably lower number of other chalcogenides.

The hatched bars in Figure 1a represent $\text{Ca}_i\text{TM}_j\text{Z}_k$ compounds with a transition metal TM of the d -block and Z any chalcogen element, i.e., $\text{O}, \text{S}, \text{Se}$ or Te . Therefore, the hatched bars exclude mixed anion moieties, such as SiO_4^{4-} , PO_4^{3-} , etc. Figure 1b presents our search strategy to identify potential Ca conductors/electrodes, with chemical formula $\text{Ca}_i\text{TM}_j\text{Z}_k$. We utilised the combined information available in the ICSD (i.e., structures and characterization conditions),⁵⁵ and the Materials Project (MP; thermodynamic stabilities)⁵⁸ to arrive at our candidates. The screening procedure, where we induce constraints on composition, redox-activity, charge-balance, and thermodynamic stability, followed the steps below:

1. *Identification of $\text{Ca}_i\text{M}_j\text{Z}_k$ compounds in the ICSD.* This initial screen could identify 412 oxides or chalcogenides $\text{Ca}_i\text{M}_j\text{Z}_k$ materials as shown in Figure 1a.
2. *Selection of $\text{Ca}_i\text{TM}_j\text{Z}_k$ compounds with a transition metal TM of the d -block,* where the TM can be redox-active. For example, even though Sc and Zn are d -block TMs, they are not known to be redox-active. As shown in Figure 1b, this important filter

could further reduce our dataset to 181 $\text{Ca}_i\text{TM}_j\text{Z}_k$ candidates, of which only 161 are oxides, 16 are sulfides and 4 are selenides (see Figure 1b). Furthermore, all 13 telluride $\text{Ca}_i\text{M}_j\text{Z}_k$ compounds were entirely made by mixed anion species (e.g., TeO_6^{2-}) and are eliminated from our selection. In this step we also eliminated all $\text{Ca}_i\text{TM}_j\text{Z}_k$ that were characterized under non-ambient conditions.

3. *Identification of discharged compositions $\text{Ca}_i\text{TM}_j\text{Z}_k$, which can be matched by charge-balanced decalciated compositions TM_jZ_k .* As Ca is deintercalated from a $\text{Ca}_i\text{TM}_j\text{Z}_k$, either partially or fully, it is important that the TM species exhibits oxidation states that are physically plausible, hence ensuring charge-neutrality of the deintercalated composition. For example, CaVO_3 is a well-known Ca-containing orthorhombic perovskite that satisfies the chemical formula of $\text{Ca}_i\text{TM}_j\text{Z}_k$ and contains an open-shell transition metal (i.e., V^{4+}). However, the fully-charged version of CaVO_3 , namely, VO_3 , requires V to exhibit an oxidation state of $6+$, which is not physical. Thus, CaVO_3 does not qualify as a candidate across this filter. Note that charge-neutrality is one of the necessary, but not sufficient, conditions for thermodynamic stability. Hence, during this filtering process, we tried to identify possible charge-neutral deintercalated composition(s) for every $\text{Ca}_i\text{TM}_j\text{Z}_k$ considered. In particular, we checked the availability of ordered structures of both fully (TM_jZ_k) and partially ($\text{Ca}_{1<i}\text{TM}_j\text{Z}_k$) deintercalated compositions that were charge-neutral in the ICSD as well as Materials Project. Although any of the screened Ca chemistries may allow partial decalciation, we preferred fully charged structures in all possible cases, since that maximizes theoretical capacities. We only considered partially decalciated compositions when ordered structure(s) were available at such compositions: else, the computational costs become intractable. Specifically, only two specific cases of partial Ca extraction came through our search, namely, CaV_2O_6 and $\text{Ca}_3\text{Cu}_6\text{O}_{12}$. Also, for the two eventual candidates proposed in this work, CaNb_2O_4 and CaV_2O_4 , we did consider some Ca configurations at partial decalciation, as illustrated by the voltage curves plotted in Figure S1 of the Support-

ing Information (SI). Wherever possible, we have identified discharge/charge structure pairs that would enable a topotactic Ca (de)intercalation. If the charged composition exhibits multiple polymorphs, we only consider the structure that topotactically matches the discharged structure and the ground state structure (if different from topotactically-matched structure) for further calculations. After this step, the number of possible $\text{Ca}_i\text{TM}_j\text{Z}_k$ electrodes further reduced to 66.

4. *Identification of final set of 10 materials to investigate with first-principles calculations.*

We arrived at our final set by eliminating all the $\text{Ca}_i\text{TM}_j\text{Z}_k$ structures which appeared thermodynamically unstable, as quantified by the 0 K energy above the convex hull (E^{hull}) that is available on MP, on their respective compositional phased diagrams. We assumed the $\text{Ca}_i\text{TM}_j\text{Z}_k$ compounds to be unstable if their $E^{\text{hull}} > 30 \text{ meV atom}^{-1}$, which has been widely accepted as a rule-of-thumb in stability-based screening studies.⁵⁹ Importantly, the availability of a thermodynamically stable $\text{Ca}_i\text{TM}_j\text{Z}_k$ compound ensures that there is no thermodynamic driving force for forming detrimental conversion products, instead of Ca-intercalation, upon reduction of the charged TM_jZ_k structure with Ca (see Table 1 and Sec. 5 for further discussion).^{10,60} Also, we did not impose any thermodynamic stability restriction on the deintercalated TM_jZ_k compositions (see discussion in Sec. 2.2).

Of the 412 $\text{Ca}_i\text{M}_j\text{Z}_k$ oxides or chalcogenides, we fully investigated the thermodynamic and kinetic properties of ten candidates and subsequently identified two structures as promising Ca conductors/electrode materials that merit further experimental investigation, namely CaV_2O_4 and CaNb_2O_4 . A comprehensive list of all the materials investigated in this study is provided in Table S1 of the SI.

2.2 Ca Intercalation Characteristics in $\text{Ca}_i\text{TM}_j\text{Z}_k$ Materials

Table 1 summarizes the intercalation characteristics of the 10 $\text{Ca}_i\text{TM}_j\text{Z}_k$ candidates, including the space groups, the ICSD or MP IDs, and E^{hull} of the discharged and charged states, the average Ca topotactic intercalation voltage (Eq. 2), the gravimetric capacity, and the specific energy (calculated from the theoretical average voltage) for all charged-discharged pairs. Table 1 also contains the Ca coordination number and the Ca E_m in the discharged state, as well as the current cost of the raw TMs in the $\text{Ca}_i\text{TM}_j\text{Z}_k$ compounds. We included CaV_2O_5 as the 11th compound in the list as a benchmark for our computational method. Overall, the screened set of ten compounds in Table 1 consists of only two sulfides (CaCu_2S_2 - Cu_2S_2 and CaMo_6S_8 - Mo_6S_8), with the rest being oxides, testament to the significantly larger collection of available oxides that naturally form with Ca in preference to other chalcogenides. All E_m reported in Table 1 are calculated to represent the discharged structure, i.e., in the dilute Ca-vacancy limit. Also, Table 1 includes both topotactic (T) and non-topotactic (N) average intercalation voltages, where relevant.

A quick glance of Table 1 reveals that all but four discharged compounds exhibit $E^{\text{hull}} = 0$ meV/atom. Three of the metastable $\text{Ca}_i\text{TM}_j\text{Z}_k$ compounds show a $E^{\text{hull}} < 30$ meV/atom (i.e., CaV_3O_7 , $\text{Ca}_5\text{Cu}_6\text{O}_{12}$ and CaMo_6S_8). Among the 10 discharged-charged pairs considered, the charged compounds can be metastable in their respective phase diagrams. For example, the deintercalated Chevrel-phase is theoretically expected to decompose as $\text{Mo}_6\text{S}_8 \rightarrow 2\text{MoS}_2 + \text{Mo}$ (~ -88.0 kJ mol⁻¹ and -908 meV). However, the Chevrel cathode has shown reversible intercalation of various ions over several cycles,⁶¹⁻⁶³ indicating that the charged Chevrel phase is kinetically stabilized in such cases. Nevertheless, reversible Ca intercalation into the Chevrel cathode has not been yet reported so far experimentally despite previous theoretical works^{64,65} comparing the intercalation behavior of Ca to other ions, suggesting possible instability associated with topotactic Ca insertion into the Chevrel. In any case, the thermodynamic metastability of charged compounds may not represent a significant deterrent for the reversible operation of a Ca battery or the ability to experimentally synthesize

Table 1: Computed characteristics of the 10 discharged $\text{Ca}_i\text{TM}_j\text{Z}_k$ and charged TM_jZ_k compounds resulting from our screening. The ICSD or MP ID of each material is provided. E^{hull} , Voltage, Capacity (Cap.), Specific energy (Spec.) and cost of transition metal are reported in units of meV/atom, Volts vs. Ca/Ca^{2+} , mAh/g, Wh/kg and \$/kg, respectively. Mech. indicate whether Ca intercalation follows a topotactic (T) or a non-topotactic (N) mechanism. The average coordination number (CN) of Ca^{2+} and the computed E_m (in meV) in the discharged structures (i.e., dilute vacancy limit) are also reported.

Material	ICSD/MP	Space Group	Mech.	E^{hull}	CN	E_m	Voltage	Cap.	Spec.	Cost
CaV_3O_7	2507	$Pnma$	–	2	7	2,892	–	–	–	–
V_3O_7	mvc-13330	$Pnma$	T	51	–	–	3.34	176	587	17.40 ^a
V_3O_7	mp-622640	$C2/c$	N	8	–	–	3.11	–	547	–
$\text{Ca}_2\text{V}_2\text{O}_6$	237336	$Pnma$	–	0	7	3,235	–	–	–	–
CaV_2O_6	This work ^d	$Pnma \rightarrow Pmn2_1$	T	95	–	–	2.96	193	571	17.40 ^a
CaV_2O_6	21064	$C2/m$	N	0	–	–	2.46	–	474	–
CaV_2O_4	164185	$Pnma$	–	0	8	654	–	–	–	–
V_2O_4	mp-777479	$Pnma$	T	26	–	–	2.40	260	624	17.40 ^a
V_2O_4	10141	$P4_2/mnm$	N	0	–	–	2.34	–	608	–
CaNb_2O_4	88779	$Pbcm$	–	0	6	785	–	–	–	–
Nb_2O_4	This work ^d	$Pbcm \rightarrow Pmma$	T	308	–	–	2.71	185	501	30.20 ^b
Nb_2O_4	96	$I4_1/a$	N	0	–	–	1.78	–	329	–
$\text{Ca}_5\text{Cu}_6\text{O}_{12}$	91059	$P2_1/c$	–	28	6	–	–	–	–	–
$\text{Ca}_3\text{Cu}_6\text{O}_{12}$	This work ^d	$P2_1/c \rightarrow P2_1$	T	92	–	–	3.19	139	443	8.75 ^c
$\text{Ca}_3\text{Cu}_6\text{O}_{12}$	mp-1540145	$I4_1/a$	N	0	–	–	2.83	–	393	–
CaMoO_3	246082	$P2_1/c$	–	0	8	2,072	–	–	–	–
MoO_3	mp-18856	$P2_1/c$	T	0	–	–	2.77	291	806	24.75 ^c
MoO_3	35076	$Pnma$	N	39	–	–	2.76	–	803	–
CaIrO_3	420479	$Cmcm$	T	0	8	–	–	–	–	–
IrO_3	mp-1097041	$Cmcm$	–	0	–	1,219	3.29	191	629	193,000.00 ^c
CaRh_2O_4	170597	$Pnma$	–	0	8	1,110	–	–	–	–
Rh_2O_4	This work	$Pnma$	T	67	–	–	2.84	173	491	860,000.00 ^c
Rh_2O_4	28498	$P4_2/mnm$	N	0	–	–	2.63	–	455	–
CaCu_2S_2	241336	$P\bar{3}m1$	–	0	6	1,622	–	–	–	–
Cu_2S_2	This work ^d	$P\bar{3}m1 \rightarrow C2/m$	T	108	–	–	2.17	232	503	8.75 ^c
Cu_2S_2	63328	$Cmcm$	N	0	–	–	1.95	–	452	–
CaMo_6S_8	619423	$R\bar{3}$	T	17	8	–	–	–	–	–
Mo_6S_8	86788	$R\bar{3}$	–	66	–	–	–	–	–	–
$\alpha\text{-CaV}_2\text{O}_5^e$	82689	$Pmnn$	T	0	8	–	–	–	–	–
V_2O_5	15798	$Pmnn$	–	0	–	1,869	3.13	241	757	17.40 ^a

^aVanadium price obtained from <https://www.vanadiumprice.com> and sold as V_2O_5 .

^bNiobium price obtained from <https://www.niobiumprice.com> and sold as Nb_2O_5 .

^cMetal prices obtained from <https://www.dailymetalprice.com/>.

^dUpon topotactic extraction of Ca^{2+} , the symmetry of the charged structure becomes different from the discharged structure.

^eConsidered as a calibration compound.

such compounds.

Unsurprisingly, from Table 1, we realize that the largest intercalation voltages are achieved by Vanadium-containing phases, which can be attributed to higher (more positive) standard reduction potential for V (e.g., $\text{V}^{\text{IV}}/\text{V}^{\text{III}} + 0.34$ V vs. SHE) compared to the other transition

metals considered (e.g., $\text{Mo}^{\text{IV}}/\text{Mo}^{\text{III}}$ -0.01 V vs. SHE).⁶⁶ Indeed, Ca intercalates in V_3O_7 and $\alpha\text{-CaV}_2\text{O}_5$ with ~ 3.34 and ~ 3.13 V vs. Ca/Ca^{2+} , respectively, significantly higher than MoO_3 (~ 2.77 V), Nb_2O_4 (~ 1.79 V), Cu_6O_{12} (~ 2.83 V), or Rh_2O_4 (~ 2.63 V). The lower voltage exhibited by V_2O_4 (~ 2.40 V) relative to the V_3O_7 and V_2O_5 frameworks can be attributed to the lower (more negative) reduction potential of the $\text{V}^{\text{IV}}/\text{V}^{\text{III}}$ than $\text{V}^{\text{V}}/\text{V}^{\text{IV}}$.

The predicted Ca intercalation voltage in V_2O_5 is in excellent agreement with previous reports,^{37,67,68} providing credibility to our methodology. The large Ca intercalation voltages and the accessibility to several stable oxidation states makes the Vanadium phases the most attractive in terms of gravimetric capacities and specific energy density, as shown in Table 1. Also, our screening reveals other promising, previously unreported phases, including *i*) the CaIrO_3 (~ 3.29 V vs. Ca/Ca^{2+}), *ii*) $\text{Ca}_5\text{Cu}_6\text{O}_{12}$, and *iii*) CaRh_2O_4 . We do not expect Ir and Rh compounds to be competitive with V compounds due to the significantly high cost of the raw metals.

During (de)intercalation, if the host framework (i.e., TM_jZ_k) does not phase transform, resulting in the symmetry of the host lattice being preserved, the (de)intercalation process is said to be topotactic. However, several cathode materials, among those that we have considered, are expected to undergo phase transformations upon Ca deintercalation, which can result in a different structure (and/or symmetry) of the charged TM_jZ_k compared to the discharged $\text{Ca}_i\text{TM}_j\text{Z}_k$ compound. Upon Ca extraction CaNb_2O_4 is thermodynamically driven to transform from the orthorhombic (space group: $Pbcm$) to tetragonal ($I4_1/a$) (see Table 1). For battery operation, topotactic intercalation mechanisms are preferred since phase transformations can lead to undesired straining (and/or fracture) of cathode particles, resulting in impedance build-up and even loss of electrochemical activity. In general, non-topotactic intercalation mechanisms are caused by the high instability of the topotactic charged phase (e.g., $\delta\text{-V}_2\text{O}_5$ for Ca) with respect to the corresponding (more stable) non-topotactic charged phase ($\alpha\text{-V}_2\text{O}_5$ for Ca). Hence, the lower the difference in stability between the topotactic and non-topotactic phases, which can be quantified by the difference between the topotac-

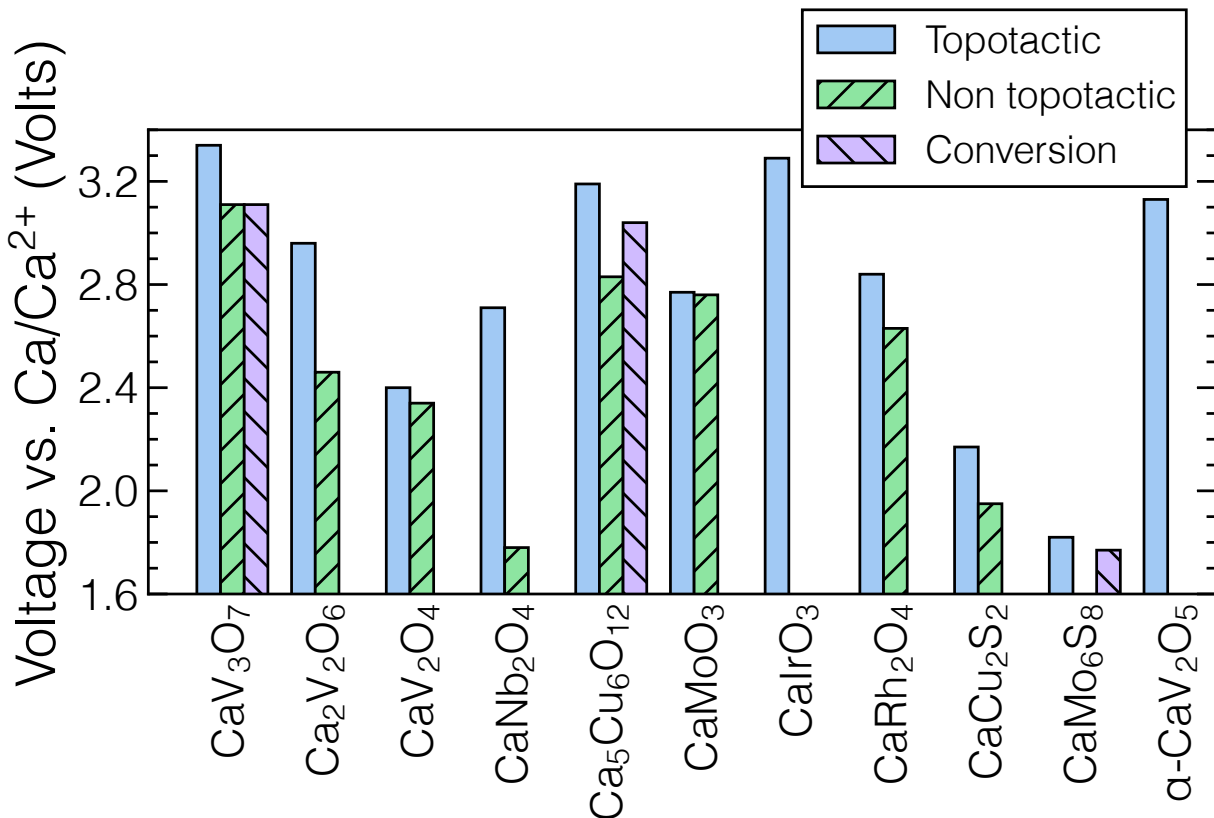


Figure 2: Computed intercalation voltages vs. Ca/Ca^{2+} of compounds in Table 1. Light-blue and hatched green bars indicate voltages associated with topotactic and non-topotactic intercalation, respectively. Missing bars indicate the unavailability of non-topotactic TM_jZ_k compounds in the ICSD or MP. The competitive conversion reactions are shown as purple hatched bars. The conversion voltage of the Chevrel phase $\text{Mo}_6\text{S}_8 + 2\text{Ca} \rightarrow 3\text{MoS}_2 + 3\text{Mo} + 3\text{CaS}$ is comparable to the topotactic insertion voltage, which is due to Mo_6S_8 being thermodynamically unstable ($\sim 66 \text{ meV } E^{\text{hull}}$, Table 1).

tic and non-topotactic voltages, the lower the tendency for a host framework to adopt a non-topotactic mechanism.

We have highlighted the difference between the topotactic (light-blue bar) and non-topotactic (green hatched bar) computed intercalation voltages for all ten identified candidates (and $\alpha\text{-V}_2\text{O}_5$) in Figure 2. Importantly, the largest difference between topotactic and non-topotactic voltage is observed in $\text{CaNb}_2\text{O}_4 \rightarrow \text{Nb}_2\text{O}_4$ of $\sim 1.0 \text{ V}$, with other compounds showing smaller differences between the two voltages. Note that even in frameworks presenting a significant difference between the topotactic and non-topotactic voltages (i.e., a few

tenths of a V), the topotactic mechanism may remain active since, this process is typically kinetically favoured over the non-topotactic intercalation. For example, the $Pnma$ phase of CaV_2O_4 is experimentally reported, but the charged $Pnma\text{-V}_2\text{O}_4$ phase is metastable (by ~ 26 meV/atom) than the stable $P4_2/mnm\text{-V}_2\text{O}_4$ phase, leading to a topotactic (non-topotactic) voltage of ~ 2.40 V (~ 2.34 V) vs. Ca/Ca^{2+} (see Figure 2). Given the small change between the topotactic and non-topotactic voltages for V_2O_4 , we speculate that the $Pnma\text{-V}_2\text{O}_4$ polymorph may benefit from kinetic stabilization. The conversion voltage upon discharge in $\text{Ca}_3\text{Cu}_6\text{O}_{12}$ (purple bar), is higher than the non-topotactic intercalation voltage, in agreement with the metastability of the discharged $\text{Ca}_5\text{Cu}_6\text{O}_{12}$ structure (Table 1). In the case of CaV_3O_7 , the conversion voltage is only marginally higher than non-topotactic intercalation voltage, as indicated by the marginal instability of V_3O_7 ($E^{\text{hull}} \sim 2$ meV/atom). However, given the larger topotactic intercalation voltage, we can expect the topotactic intercalation reaction to be kinetically favored in both the $\text{Ca}_5\text{Cu}_6\text{O}_{12}\text{-Ca}_3\text{Cu}_6\text{O}_{12}$ and $\text{CaV}_3\text{O}_7\text{-V}_3\text{O}_7$ systems. Nevertheless, topotactic (de)intercalation in multivalent systems are in general more complex than monovalent (Li/Na) systems,^{10,11} as highlighted by recent studies that have demonstrated decomposition reactions upon Ca extraction in CaTaN_2 ,⁴³ and phase transformations upon Ca removal in $\text{Ca}_3\text{Co}_2\text{O}_6$.⁶⁹

2.3 Ca^{2+} Migration Barriers

Excluding Mo_6S_8 that has already been studied extensively as a multivalent cathode,¹⁰ we computed the migration barriers for Ca^{2+} E_m for the remaining 9 materials of Table 1. All computed migration energy paths shown in Section S4 of the SI. We have calculated the E_m for all materials assuming the dilute vacancy limit, where Ca migration occurs via a vacancy-migration mechanism, unless otherwise specified. Despite our best efforts, we were unable to converge the E_m for $\text{Ca}_5\text{Cu}_6\text{O}_{12}$ structure and thus have not reported its E_m in this work. Notably, our computed E_m of 1869 meV in $\alpha\text{-CaV}_2\text{O}_5$ (see Figure S10 in SI) is in excellent agreement with a previous calculation (~ 1900 meV) done in the dilute vacancy

limit.³⁷

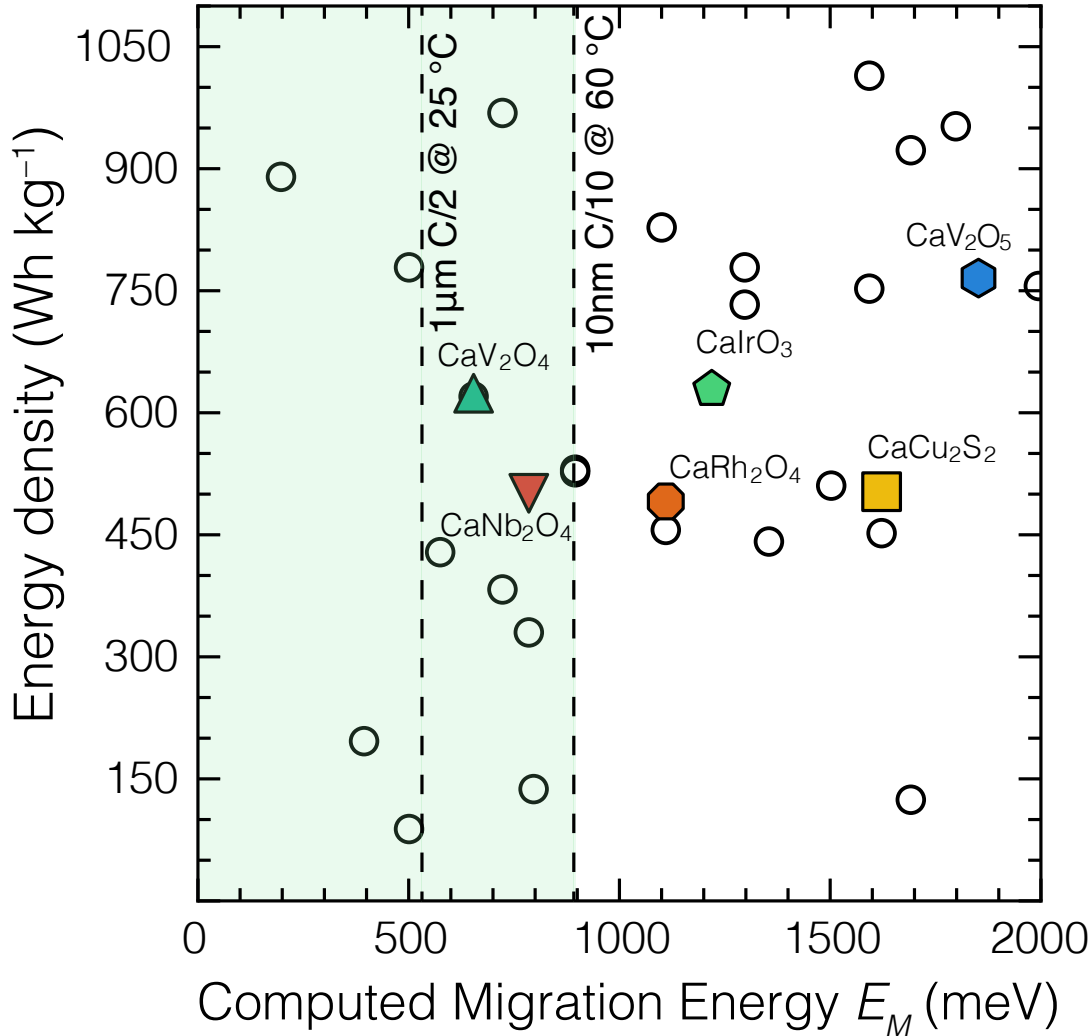


Figure 3: Computed Ca²⁺ migration barriers (in meV) plotted with respect to the predicted specific energies (in Wh kg⁻¹). Coloured points are materials investigated in this study, empty circles are computationally predicted data points from Ref. 11. The green ribbon shows favourable Ca²⁺ migration barriers. Reported energy densities rely on topotactic intercalation voltages, which indicate the most probable Ca insertion reactions. Specific tolerable migration barriers (i.e., 525 and 895 meV) at specific (dis)charge conditions are marked by dashed lines.^{10,32,33} Materials considered in our study that exhibit barriers above 2000 meV (CaV₃O₇, Ca₂V₂O₆, and CaMoO₃) are not shown in the figure.

Figure 3 shows the computed Ca migration barriers in selected materials (see coloured shapes) vs. their predicted specific energies (y-axis). Black empty circles in Figure 3 indicate

previously reported E_m for different materials from Arroyo-de Dompablo and collaborators,¹¹ which serve as useful reference points for our candidates. The green region in Figure 3 marks the range of tolerable migration barriers E_m . In Figure 3, dashed lines at ~ 525 meV and at ~ 895 meV correspond to Ca (de)intercalation across a micron-sized cathode particle at 298 K and C/2 rate, and Ca (de)intercalation across a 10 nm cathode particle, at 333 K (~ 60 °C) and C/6 rate (6 hours), respectively.^{10,32,33} The variation of the maximum tolerable E_m vs. particle size, C-rate, and temperature is given in Figure S2 of the SI.

Three main observations can be made from Figure 3 and Table 1: *i*) the computed barriers for all these materials are found to be larger than the ~ 650 meV threshold of Rong et al.,³² with $\text{Ca}_2\text{V}_2\text{O}_6$ displaying the largest E_m of ~ 3235 meV, *ii*) of the ten materials investigated, only two materials CaNb_2O_4 (~ 785 meV) and CaV_2O_4 (~ 654 meV) qualify the mobility criterion since their predicted E_m are under the highest threshold of 895 meV, and *iii*) the specific energy of CaV_2O_4 is quite competitive with other compounds previously reported by Arroyo-de Dompablo et al.,¹¹ and far exceeds commercial Li-ion cathodes.⁸ Although eight out of the ten shortlisted candidates display exceedingly large Ca^{2+} migration barriers, we believe there is value in communicating these high E_m values to not only focus experimental effort on the promising candidates but also to reformulate the design rules that can aid in designing better Ca-conductors.

2.4 Assessment of CaV_2O_4 and CaNb_2O_4 electrodes

***Pnma*- CaV_2O_4 , post-spinel:** The structure of CaV_2O_4 arranges in the post-spinel-type prototype (also referred as the calcium ferrite structure), where the vanadium resides in distorted edge-sharing and corner-sharing VO_6 octahedral units (Figure 4a). The post-spinel structure has been described in detail elsewhere,⁷⁰ where Mg occupies an 8-coordinated site in the post-spinel $\text{Mg}_x\text{V}_{2-y}\text{Ti}_y\text{O}_4$. Similarly, CaV_2O_4 exhibits Ca^{2+} in an 8-coordinated environment with Ca-migration occurring along 1D channels in the c direction (see Figure 4a). Therefore, *Pnma*- CaV_2O_4 is a 1D conductor, leading to a migration topology of

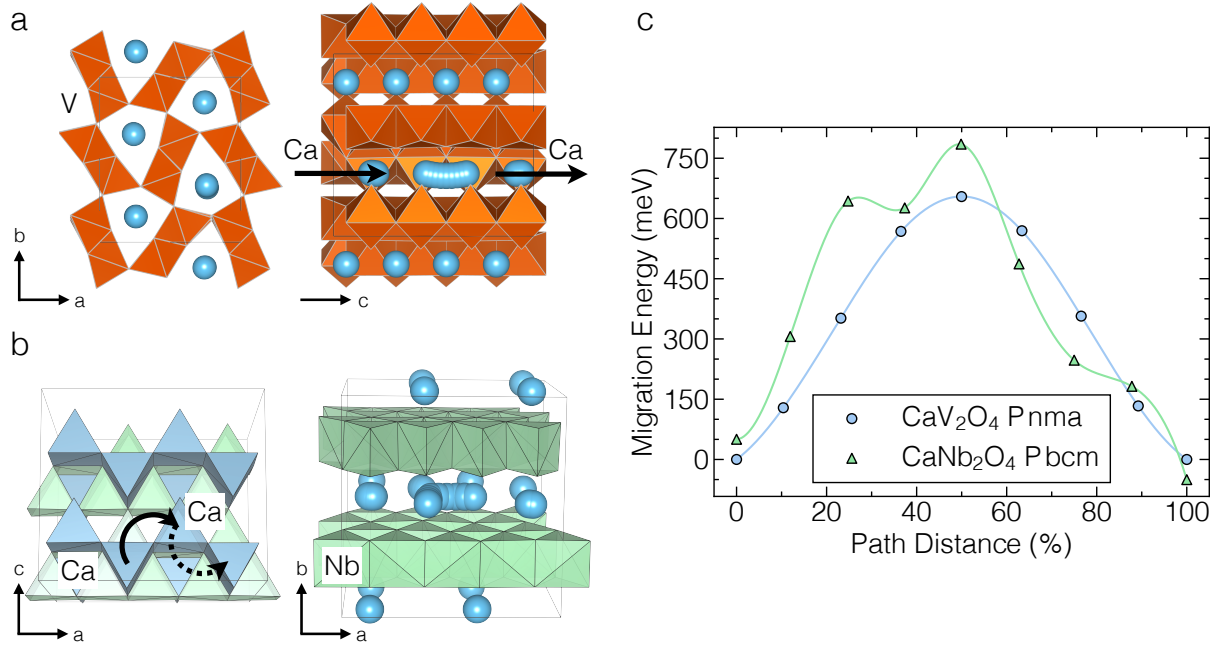


Figure 4: Panels (a) and (b) show the structural features of CaV_2O_4 (with space group: $Pnma$) and CaNb_2O_4 ($Pbcm$) highlighting the Ca^{2+} migration path. V and Nb polyhedra are depicted in orange and green, respectively, while Ca is shown either as blue spheres or polyhedra. Arrows indicates the direction of Ca^{2+} migration. (c) Computed migration energy paths (in meV) of CaV_2O_4 (blue circles) and CaNb_2O_4 (green triangles) vs. Ca^{2+} displacement.

$8 \rightarrow 5 \rightarrow 3 \rightarrow 5 \rightarrow 8$ between two equivalent Ca sites. The migration energy path of Figure 4c reaches its maximum (~ 654 meV) when Ca is in a 3-coordinated (triangular) site. Post-spinel structures have been previously considered for Ca intercalation. For example, de Dompablo et al.⁴⁷ have studied Ca intercalation in the CaMn_2O_4 (CM)- and CaFe_2O_4 (CF)-type post-spinel structures of CaMn_2O_4 composition.

$Pbcm$ - CaNb_2O_4 , layered: In CaNb_2O_4 , Nb atoms are 6-coordinated by oxygens forming edge-sharing, distorted triangular NbO_6 prisms, which give rise to the layered structure in Figure 4b. Ca^{2+} -ions occupy an ordered configuration of 6-coordinated irregular prismatic sites residing in-between the NbO_6 layers. Therefore, CaNb_2O_4 can be considered as a 2D-conductor. The in-layer migration of Ca^{2+} follows a topology $6 \rightarrow 4 \rightarrow 6$, with a maxima of

~ 785 meV at the 4-coordinated (rectangular) site, as indicated by Figure 4c. As highlighted by the solid and dash curved arrows of Figure 4b, we have calculated the migration barrier from half the total path, which explains the difference between the energies of the ground-state structures (at 0 and 100 %, Figure 4c).

3 Discussion

So far, the identification of promising intercalation cathode materials has been limited by the relatively large ionic size of Ca^{2+} , which decreases the availability of structural framework compatible with hosting and transporting Ca^{2+} ions.⁷¹ In this report, we have searched the chemical space of ternary $\text{Ca}_i\text{TM}_j\text{Z}_k$ compositions using a combination of existing databases, intuitive filtering criteria, and DFT calculations. From an initial pool of 412 Ca-containing materials found in the ICSD, we shortlisted 10 promising candidates, whose intercalation properties were assessed further via *ab initio* methods. Our screening strategy (of Figure 1) is robust as it also provides known candidates that have been previously studied experimentally (and computationally) as Ca-cathodes. While TiS_2 has been demonstrated to intercalate reversibly Ca^{2+} ,^{41,42} our screening criteria could not reveal this compound, as a stoichiometric calciated structure, i.e., Ca_xTiS_2 , is presently unknown. However, the robustness of our strategy is validated by the re-discovery of chevrel- Mo_6S_8 and CaMoO_3 phases that have received attention as Ca-electrodes.^{44,48,53} Our screening procedure did not identify the following compounds which have been studied computationally before: $\text{Ca}_4\text{Fe}_9\text{O}_{17}$ has a low $E_m \sim 720$ meV⁵² but does not have a matching, ordered, charged structure, and $\text{Ca}_3\text{Co}_4\text{O}_9$ exhibits $E_m \sim 900$ meV⁵¹ but is significantly unstable ($E^{\text{hull}} \sim 73$ meV/atom⁵⁸). Furthermore, we did not consider $\text{Ca}_3\text{Co}_2\text{O}_6$ as a possible candidate since previous experimental studies have reported the structure to undergo an irreversible phase transformation upon Ca extraction.⁵¹

Using a different computational screening strategy, Zhang et al.⁷² did consider CaNb_2O_4

as a possible intercalation electrode for Ca batteries. Unfortunately, the authors discarded CaNb_2O_4 on the basis of the high computed E_m (~ 2100 meV) in their work. We believe that Zhang et al.⁷² computed the E_m for Ca migration through the sterically-constrained O–O dumbbell that is shared between adjacent prismatic sites instead of considering the migration mechanism via a quadrilateral planar (see Section 3.2 for more detailed explanation) transition state. Ca migration through the O–O dumbbell may have been caused due to one or both of the following reasons: *i*) the authors attempted to calculate the full migration path, thereby not having an additional Ca-vacancy that can aid migration (see Figure 4b), and *ii*) the authors did not initialize their nudged elastic band (NEB⁷³) calculation via the quadrilateral planar transition state.

Given the scarcity of known good Ca conductors,¹¹ our strategy emphasises the identification of compounds providing facile Ca transport, apart from our criteria including the availability of charged structures and overall thermodynamic stability, while Zhang et al.’s strategy prioritized Ca-intercalation voltages and capacities,⁷² which tends to overlook more practical candidates.

3.1 Established design rules to identify good ionic conductors

It is important to take a look at the three rules to identify good multivalent conductors, initially proposed by Rong et al.,³² and examine their applicability with our findings (see Table 2 for a summary). Note that the rules were initially devised for the discovery of good Mg candidates and had not been extensively tested in Ca containing compounds. The rules are:

1. *Avoid host structure where the active ion, Ca^{2+} , resides in its preferred anion coordination environment.* A previous statistical analysis of the ICSD^{54,55} showed that Ca^{2+} highly prefers a coordination number of 8 and above in oxides.⁵⁶ The preferred coordination environment of Ca^{2+} in chalcogenides, such as S, Se, and Te, has not been yet quantified rigorously. As a result, a good Ca^{2+} conductor should display a

Ca coordination number < 8 in oxides according to this rule. However, one of the two good conductors that we have found in our search, CaV_2O_4 does have Ca residing in an 8 coordination environment. In contrast, CaCu_2S_2 exhibits a high E_m (~ 1622 meV) despite Ca occupying an un-preferred octahedral environment. With respect to the limited number of structures considered in this study, this rule does not seem to be a good classifier of good vs. bad Ca diffusers. Hence, it is important to update this rule by examining its applicability on an even larger and more diverse dataset.

2. *Reduce changes in the coordination number of the active ion (Ca^{2+}) during its migration.* This rule proposes that smaller changes in coordination environment along the migration path of Ca^{2+} flattens the potential energy landscape, in turn reducing E_m .^{32,35} We could find several exceptions to this rule in the set of materials that we have considered. For example, CaV_2O_4 , CaIrO_3 , CaRh_2O_4 , CaMoO_3 and CaV_2O_5 have similar coordination number change from stable to transition state (i.e., $8 \rightarrow 3$), yet display widely different migration barriers (654–2072 meV). CaV_3O_7 , $\text{Ca}_2\text{V}_2\text{O}_6$, and CaCu_2S_2 all have relatively low changes in coordination number, namely $8 \rightarrow 5$, $8 \rightarrow 4$, and $6 \rightarrow 4$, than CaV_2O_4 , yet exhibit significantly higher barriers (> 1600 meV vs. 654 meV). Thus, reducing coordination changes alone does not seem to be reducing the E_m in Ca compounds.

3. *Increase the available volume (per number of anions) to Ca^{2+} in a given framework.* In “compact” frameworks, larger volumes per anion typically correlate with weaker electrostatic interactions of Ca^{2+} with the anion (and other cations) and promote a reduction of E_m .^{32,35} Generally, larger volumes per anion can be obtained by going from oxides to sulfides (or other chalcogenides) in the same structural framework.^{35,74} This rule may not directly apply to non-compact structures, where the active ion resides in tunnel-type (e.g., hollandite MnO_2) arrangements. Here, we obtain a high barrier of 1622 meV in compact layered- CaCu_2S_2 despite a sulfide anion framework. While the

oxide analogue CaCu_2O_2 structure has not been reported and we cannot perform a direct barrier comparison with CaCu_2S_2 , some of the post-spinel oxides (e.g., CaV_2O_4 and CaRh_2O_4) exhibit a lower barrier than CaCu_2S_2 , despite being compact frameworks (post-spinel phases are typically stable at high pressures⁷⁰).

In summary, we observe that the above rules may not be applicable to large cation⁷⁵ migration, e.g., K^+ ($\sim 1.64\text{--}1.46$ Å), Rb^+ ($\sim 1.83\text{--}1.52$ Å), Cs^+ ($\sim 1.67\text{--}1.88$ Å) and Ca^{2+} ($\sim 1.34\text{--}1.00$ Å). In particular, rule No. 1 was derived based on observations in compact anion lattices and cannot account for the diversity of geometrical and electrostatic factors appearing in more complex motifs, such as those sampled in our study. For example, it is known that Ca^{2+} does not occupy sites usually occupied by Li^+ or Na^+ in LiFePO_4 or NaFePO_4 ,³⁶ which is attributed both to the site preference of Ca and the underlying flexibility of the host structure to accommodate Ca. We attempt to revise the design rules for identifying good conductors, especially for frameworks with large mobile cations, in the following section.

3.2 Revised design rules for identifying good ionic conductors

Table 2: Geometric features of the stable and transition states are listed along with the E_m (in meV) for materials considered in this work. Avg. BL represents the average Ca-anion bond-length in the stable state (in Å). D/A/V stand for diagonal or area or volume at the transition state and in units of Å, Å², and Å³, respectively. y_{Ca} represents the fraction of diagonal/area/volume of the transition state occupied by Ca. Final column indicates any presence of a face-sharing cation at the transition state.

Material	E_m	Stable state	Avg. BL	Transition state	D/A/V	y_{Ca}	Face-sharing cation?
CaV_3O_7	2892	Augmented triangular prism	2.44	Rectangular pyramid	7.10 ^v	0.83	1 V at 2 Å
$\text{Ca}_2\text{V}_2\text{O}_6$	3235	Biaugmented triangular prism	2.51	Square planar	3.36 ^a	0.67	N/A
CaV_2O_4	654	Biaugmented triangular prism	2.45	Triangular	4.56	0.86	N/A
CaNb_2O_4	785	Triangular prism	2.39	Rectangular	4.42 ^a	0.51	N/A
CaMoO_3	2072	Biaugmented triangular prism	2.55	Triangular	3.82	1.03	N/A
CaIrO_3	1219	Biaugmented triangular prism	2.46	Triangular	4.32	0.91	N/A
CaRh_2O_4	1110	Biaugmented triangular prism	2.46	Triangular	4.32	0.91	N/A
CaCu_2S_2	1622	Octahedron	2.83	Tetrahedron	7.55 ^v	0.78	1 Cu at 1.57 Å
$\alpha\text{-CaV}_2\text{O}_5$	1869	Distorted square antiprism	2.50	Triangular	3.70	1.06	N/A

^aShortest diagonal length reported.

^vVolumetric (3D) transition state.

Our motivation to formulate new design rules primarily arises from the following observations among the calculated E_m in this work. Specifically, *i)* Materials with similar structures and Ca coordination environments (at both stable and transition states) exhibit significantly different E_m . For example, CaV_2O_4 and CaRh_2O_4 are both post-spinel structures but show barriers that differ by nearly ~ 400 meV. *ii)* On the other hand, materials that indeed show similar barriers exhibit remarkably different structures, such as CaV_2O_4 and CaNb_2O_4 , CaIrO_3 and CaRh_2O_4 , and CaMoO_3 and CaV_2O_5 . *iii)* The reasons for CaV_3O_7 and $\text{Ca}_2\text{V}_2\text{O}_6$ to exhibit the highest barriers among the materials considered here, are not immediately obvious.

We decided to take a deeper look into the geometrical features of the stable and transition states in the structures considered here, and our findings are summarised in Table 2. Note that our analysis is biased by the limited number and diversity of structures that we have sampled and also excludes other thermodynamic (e.g., stability or energy above the convex hull) and electronic (e.g., metallic vs. non-metallic) properties that can influence E_m . A larger dataset of migration energy profiles across a wider range of structures is required to fully understand and decouple the different contributions to E_m , which is beyond the scope of this work.

The biaugmented triangular prism and distorted square antiprism in Table 2 correspond to 8-coordinated (stable) sites of Ca and the augmented triangular prism refers to a 7-coordinated site. Avg. BL (in Å) refers to the average Ca-anion bond-length in the stable site of each structure. While triangular, rectangular, and square planar are 2D (planar) transition states, rectangular pyramid and tetrahedron are 3D (volumetric). D, A, V in Table 2 represent the length of the diagonal (in Å) for a quadrilateral transition state, the area (in Å²) of a triangular transition state, and the volume (in Å³) of a volumetric transition state (i.e., a three-dimensional or a 3D space), respectively. y_{Ca} represents the fraction of the diagonal/area/volume occupied by Ca at the transition state and the final column of Table 2 indicates the presence (or not) of a face-sharing cation and its distance from the migrating

Ca, at a volumetric transition state. For identifying the number of Ca-anion bonds at the transition state (and hence to calculate the geometrical features of the transition state), we used the longest Ca-anion bond-length at the stable state as the upper-limit for each structure considered.

Note that all geometrical features reported in Table 2 are obtained from a DFT-relaxed geometries of the ground states (endpoint structures). The end-point configurations are typically relaxed before doing NEB and they are not altered during the course of a NEB calculation. The features reported are for a non-migrating Ca ion, i.e., we take the DFT-relaxed endpoint structure and label a Ca-ion that is non-migrating but is symmetrically equivalent to the migrating Ca. Subsequently, we construct a (hypothetical) migration path for the labelled Ca-ion, which mimics the set of images that are used as a starting point for the NEB, locate the transition state along the as-constructed migration path and estimate the geometrical features of the located transition state. Note that we focus on a non-relaxed migration path of a non-migrating Ca-ion to ensure that we include any “global” structure relaxations (e.g., any changes in lattice parameters) of the endpoint structures while excluding any “local” structure relaxations that result from the relaxation of the endpoint configuration at the site of the migrating Ca.

We can infer from Table 2 that the most common stable and transition states are 8-coordinated and 3-coordinates sites, respectively, exhibiting a wide range in E_m from 654-2072 meV. Since the stable 8-coordinated sites do not differ significantly in terms of average BL (2.45–2.51 Å), we expect the variations in observed E_m , in such frameworks, to primarily arise from the differences in the transition state. For example, if Ca is migrating through a triangular transition state, as shown in Figure 5a, an “optimal” size of the triangular transition state will ensure a lower E_m compared to scenarios where the triangle is too expanded or too constricted.

If we assume a rigid sphere model of atoms in a framework, the optimal triangular framework is where the central Ca atom (green spheres in Figure 5a) shares common tangents

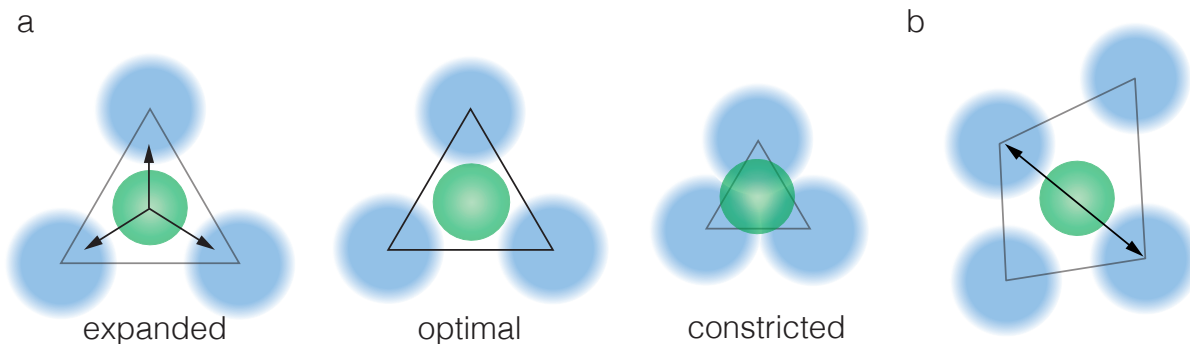


Figure 5: Ca^{2+} ions (green circles) in triangular (panel (a)) and quadrilateral (panel (b)) anion environments, which can constitute possible transition states during migration. Panel (a) classifies three types of triangular environments based on the triangular area, namely expanded, optimal, and constricted. In panel (b) the shortest diagonal of a quadrilateral transition state, along which Ca can share common tangents with anions, is shown.

with the three oxygen atoms (blue spheres) that form the vertices of the triangle. Given an ionic radius⁷⁵ of Ca^{2+} and O^{2-} to be 1.12 Å and 1.38 Å, respectively, we can calculate the fraction of the triangular area occupied by Ca (y_{Ca}) under the optimal condition to be ~ 0.48 . In the case of a triangular transition state with S^{2-} vertices (ionic radius of $\text{S}^{2-} \sim 1.84$ Å),⁷⁵ optimal y_{Ca} will be 0.35. Hence, triangular transition states that have y_{Ca} closer to the optimal value will have a lower E_m . Similar optimal conditions can be derived for other types of transition states as well. In the case of a quadrilateral-type transition state (Figure 5b), such as, square planar or rectangular, the rigid sphere of Ca^{2+} has to share common tangents with the anion vertices along the shortest diagonal. Thus, for O^{2-} and S^{2-} quadrilateral vertices, the optimal fraction of the diagonal that should be occupied by Ca^{2+} is 0.45 and 0.38, respectively. Analogously, the optimal volume fraction that Ca^{2+} should occupy in a tetrahedron with O^{2-} (S^{2-}) vertices is 0.73 (0.44), while in the case of a square pyramid, the optimal volume fraction with O^{2-} vertices is 0.28—in a square pyramid, only half of the Ca sphere will be fully contained within the pyramid. The optimal y_{Ca} in sulfide frameworks will be lower than oxide analogues due to the larger ionic radius of S^{2-} compared to O^{2-} .

We can explain important trends observed in Table 2 based on the deviation of the transition state away from the optimal condition. For example, the y_{Ca} of the triangular transition state in CaV_2O_4 is closer to the optimal triangle by ~ 0.05 than the y_{Ca} of CaRh_2O_4 , which causes a lowering of E_m by ~ 400 meV in CaV_2O_4 . Both CaV_2O_4 and CaRh_2O_4 are post-spinels with nearly-identical stable sites, which indicates the importance of the small deviations in the transition state on the overall barrier. Interestingly, y_{Ca} in CM- and CF-type post-spinels of composition CaMn_2O_4 are 0.97 and 0.91, respectively, as calculated from the corresponding DFT-relaxed bulk structures available in the MP. These y_{Ca} values are in excellent agreement with previously reported⁴⁷ E_m values, namely ~ 1850 meV in CM and ~ 1350 meV in CF CaMn_2O_4 , further validating our optimal y_{Ca} criterion. CaNb_2O_4 exhibits a quadrilateral transition state (rectangular, Figure 4b) whose y_{Ca} is closer to the optimal value by ~ 0.16 than the y_{Ca} of $\text{Ca}_2\text{V}_2\text{O}_6$, causing a lowering of ~ 2400 meV of E_m in CaNb_2O_4 . Furthermore, CaRh_2O_4 and CaIrO_3 both exhibit similar barriers (difference of ~ 100 meV) owing to similar y_{Ca} in the transition state, while the E_m of CaMoO_3 and CaV_2O_5 differ marginally (~ 200 meV) owing to the change in y_{Ca} (~ 0.03) at their triangular transition states. Although we do not expect the relationship between the deviation from optimality and E_m to be linear, we can expect a transition state that is closer to its optimality to yield a lower E_m .

The presence (or lack of) non-migrating cations, such as transition metals, or other cations, e.g., S^{6+} , P^{5+} , etc., that share a “face” with a volumetric transition state, can also have a non-negligible impact on the values of E_m . Indeed, the high barriers in CaV_3O_7 and CaCu_2S_2 can be attributed, to a large extent, to the face-sharing V and Cu atoms, respectively, at the transition state during Ca migration. Such face-sharing cations can cause a significant increase in electrostatic potential energy due to electrostatic repulsion, particularly at small separations from the migrating Ca, resulting in a higher barrier. For example, the Ca-Cu distance in CaCu_2S_2 at the transition state (~ 1.57 Å) is significantly lower than the Ca-S bond distance in the same site (~ 2.45 Å), signifying that the Ca-

Cu electrostatic repulsion is insufficiently screened by the surrounding anion framework, resulting in the high E_m (~ 1622 meV) observed. In general, we expect face-sharing cations to have a higher impact on E_m in oxides than sulfides (or other chalcogenides), in line with previous observations,⁷⁶ due to the higher ionicity of oxygen-containing bonds and the lack of electrostatic screening by O^{2-} compared to S^{2-} ,¹⁰ partly explaining the higher E_m in CaV_3O_7 than $CaCu_2S_2$. Also, there are examples of electrostatic repulsion forcing multivalent ions to migrate through a sterically-constrained anion-cation-anion dumbbell site instead of a planar or a volumetric transition site,⁷⁶ always resulting in higher barriers.

Apart from optimal transition states and face-sharing cations, we speculate that structures that exhibit a lower Ca volume fraction change (Δv_{Ca}) during migration, to yield a lower E_m . Although we do not have a rigorous set of calculated barriers to justify this suggestion, we highlight the similarities (and differences) with rule No. 2 in Sec. 3.1. For a given polyhedral coordination that Ca is occupying, v_{Ca} is the fraction of the polyhedral volume occupied by a rigid Ca^{2+} sphere. Therefore, if a migration pathway minimizes Δv_{Ca} during Ca motion (i.e., reduce the change in v_{Ca} between the stable and transition states), it should, in principle, flatten the potential energy landscape, since Ca is moving across polyhedra that are “similar”. This is analogous to what is expected by minimising changes in coordination number during migration, but results in a better metric (both quantitatively and qualitatively) to identify the similarity of polyhedral motifs during ionic migration. However, there is an inherent trade-off associated with maintaining the same v_{Ca} and attaining the optimal y_{Ca} at transition state, which will eventually decide the magnitude of E_m . This trade-off can be approximately considered to be breaking/forming the optimal number of bonds during migration.

Finally, we suggest that volumetric/planar transition states that have more degrees of freedom (DoF, i.e., number of allowed changes of edge lengths and shapes) to attain better v_{Ca} - y_{Ca} trade-offs, and result in lower E_m . Thus, we are hopeful that materials that exhibit a quadrilateral-type transition state, which has more DoF than triangular, and have E_m lower

than CaNb_2O_4 (shown in this work) will be identified in the near future.

To summarise, we propose the following updated set of design rules for identifying good ionic conductors, especially for structures with large migrating cations:

1. Find structures that yield close to the optimal diagonal/area/volume (D/A/V) fraction of migrating cation at the transition state (excluding any “local” relaxation during migration).
2. In case of volumetric transition states in frameworks, avoid face-sharing cations.
3. Minimise changes in the volume fraction of cation as it migrates across sites (by choosing structures exhibiting transition states with higher degrees of freedom).

4 Conclusion

In summary, we investigated the large compositional space of more than 400 ternary chalcogenides with prototypical formula $\text{Ca}_i\text{M}_j\text{Z}_k$. From this large pool of materials, 10 materials were studied using first-principles calculations. We found two previously unreported promising electrode candidates, namely post-spinel CaV_2O_4 and layered CaNb_2O_4 , with Ca migration barriers of ~ 654 meV and ~ 785 meV, respectively. From the analysis of the Ca migration characteristics in the 10 selected compounds, we proposed updated design rules for the identification of good Ca conductors. These rules are to find structures: *i*) with optimal diagonal/area/volume at the transition state, *ii*) without any face-sharing cations at the transition state, and *iii*) that minimise changes in polyhedral volumes during ion migration. While our study centered on Ca-based materials for positive electrodes, our findings may be extended to other compounds hosting large mobile cations.

5 Methodology

5.1 *Ab initio* Thermodynamics of Conversion and Intercalation Voltages

An intercalation battery based on the hypothetical $\text{Ca}_n\text{TM}_j\text{Z}_k$ cathode electrode implies the reversible extraction/insertion of Ca^{2+} ions from/into the $\text{Ca}_n\text{TM}_j\text{Z}_k$ framework following the spontaneous reaction of Eq. 1.



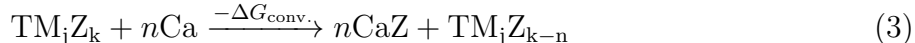
where n sets the Ca concentration and $-\Delta G_{\text{inter.}}$ is the change of Gibbs energy at 0 K, where the DFT total energies are approximated as the Gibbs energies (i.e., $E \approx G$). By doing so, we neglect the pV and entropic contributions to the Gibbs energy. From Eq. 1 we estimate the average intercalation voltage, $V_{\text{inter.}}$, as expressed in Eq. 2.

$$V_{\text{inter.}} = -\frac{\Delta G_{\text{inter.}}}{2nF} = -\frac{E_{\text{Ca}_n\text{TM}_j\text{Z}_k} - [E_{\text{TM}_j\text{Z}_k} + n\mu_{\text{Ca}}]}{2nF} \quad (2)$$

where μ_{Ca} is the Ca chemical potential (set to that of Ca metal) and F is the Faraday constant. The value 2 in the denominator of Eq. 2 takes into account the two electrons released upon oxidation of Ca to Ca^{2+} . Note that the reaction represented by Eq. 1 can be either topotactic or non-topotactic in nature. Computed intercalation voltages are reported in Table 1 and Figure 2.

An alternative process to Ca intercalation is the conversion of a hypothetical TM_jZ_k cathode upon reduction with Ca, leading typically to the irreversible formation of stable binary/ternary oxides (e.g., CaO and TMO) that can detrimentally stop any electrochemical activity. Previous studies have examined the competition between intercalation and conversion reactions in a large dataset of multivalent TM oxide, sulfide, and selenide

chemistries.^{10,60} As an example, a possible conversion reaction is shown in Eq. 3 for a hypothetical TM_jZ_k forming CaZ and $\text{TM}_j\text{Z}_{k-n}$.



A conversion voltage can be linked to such reactions, as represented by Eq. 4.

$$V_{\text{conv.}} = -\frac{\Delta G_{\text{conv.}}}{2nF} = -\frac{nE_{\text{CaZ}} + E_{\text{TM}_j\text{Z}_{k-n}} - [E_{\text{TM}_j\text{Z}_k} + n\mu_{\text{Ca}}]}{2nF} \quad (4)$$

For intercalation reactions to be thermodynamically favourable, $V_{\text{inter.}}$ needs to be higher than $V_{\text{conv.}}$. Another way to assess whether the intercalation of Ca is favoured over undesired conversion reactions is to examine the thermodynamic stability of the discharged $\text{Ca}_i\text{TM}_j\text{Z}_k$ compound with respect to a combination of all possible compounds that can exist at the same composition, which is captured by the E^{hull} . A potential cathode that exhibits $E^{\text{hull}} = 0$ meV/atom will strongly favour intercalation reactions over conversion upon reduction with Ca.

5.2 First-principles Calculations

To assess the suitability of the $\text{Ca}_i\text{TM}_j\text{Z}_k$ -type compounds for Ca electrodes, we computed the migration energy E_m using the NEB method^{73,77} together with DFT calculations.^{45,46} In DFT, the total energy was approximated by the generalized gradient approximation (GGA) exchange-correlation functional as parameterized by Perdew, Burke, and Ernzerhof (or PBE),⁷⁸ which was evaluated using the code VASP.^{79,80} The electronic wavefunctions were expanded as plane-waves up to a kinetic energy cut-off of 520 eV and combined with the projector-augmented-wave (PAW) potentials for the core electrons.⁸¹ The PAW potentials used were, Ca_sv (06Sep2000 3s3p4s), Cu (05Jan2001 d¹⁰p¹), Ir (06Sep2000 s¹d⁸), Mo_pv (08Apr2002 4p5s4d), Nb_pv (08Apr2002 4p5s4d), O (08Apr2002 2s2p), Rh (06Sep2000 s¹d⁸), S (17Jan2003 s²p⁴), and V_pv (07Sep2000 p⁶d⁴s¹). The total energies in DFT were

integrated using a k -point density of at least 1000/atom, and converged within 10^{-6} eV/cell, without imposing symmetry restrictions. The atomic forces and stresses were converged to within 10^{-2} eV/Å and 0.29 GPa, respectively.

For the estimations of the Ca intercalation voltages in $\text{Ca}_i\text{TM}_j\text{Z}_k$ compounds, which often behave as highly-correlated systems,⁸²⁻⁸⁷ we employed the rotationally invariant Hubbard U approach to GGA, as proposed by Dudarev *et al.*,⁸⁸ resulting in a GGA+ U (or PBE+ U) Hamiltonian. GGA+ U corrects for the self-interaction error introduced by the highly localized d orbitals of the redox species V, Cu, Nb, and Mo. Note that the empirical GGA+ U correction has been extensively calibrated to compute intercalation voltages in battery materials.^{82,86,87} The specific U values used were 3.10 eV for V, 4.00 eV for Cu, 1.50 eV for Nb, and 4.38 eV for Mo, as previously reported by Jain *et al.*⁸⁶

Following the prescription by Chen *et al.*,³³ we implemented model supercells that always introduced a minimum distance ≥ 8 Å between the Ca ions participating in the ion migration, to minimize the fictitious interactions between periodic images, in our NEB^{73,77,89} calculations. We fully relaxed (*i.e.*, coordinate, volume and shape) the initial and final states defining the Ca^{2+} migration paths in our NEB until the forces on the atoms were lower than 10^{-2} eV/Å⁻¹. Note that we used the GGA functional in our initial/final state and the overall NEB calculation as well, since the GGA has been shown to be more appropriate than GGA+ U to predict ion migration paths.³² The elastic bands in all materials considered is constructed using seven distinct, equally-spaced images, between the ground-state structures (*i.e.*, the endpoints). The forces on the elastic band are converged to within 0.05 eV Å⁻¹. All E_m estimations were done in the regime of dilute vacancy, *i.e.*, one vacancy is created in the Ca lattice. Notably, the introduction of Ca-vacancies in the potential electrodes (as required for NEB calculations) were compensated by the spontaneous oxidation of nearby transition metal(s).

Acknowledgement

P.C. acknowledges funding from the National Research Foundation under his NRF Fellowship NRFF12-2020-0012 and support from the Singapore Ministry of Education Academic Fund Tier 1 (R-284-000-186-133). G.S.G. acknowledges financial support from the Indian Space Research Organization-Space Technology Cell at the Indian Institute of Science, under project code number ISTC/MET/SGG/451. The computational work was performed on resources of the National Supercomputing Centre, Singapore (<https://www.nscg.sg>).

Supporting Information Available

The supporting information contains: *i*) The structural and thermodynamic stabilities of 412 ternary chalcogenides, *ii*) A model showing the maximum tolerable migration barrier vs. particle size, rate, and temperature, and *iii*) The computed migration energy profiles of ternary chalcogenides considered.

References

- (1) Tarascon, J.-M. *Nat. Chem.* **2010**, *2*, 510–510.
- (2) Noorden, R. V. *Nature* **2014**, *507*, 26–28.
- (3) Larcher, D.; Tarascon, J.-M. *Nat. Chem.* **2015**, *7*, 19–29.
- (4) Nykvist, B.; Nilsson, M. *Nat. Clim. Change* **2015**, *5*, 329–332.
- (5) Cano, Z. P.; Banham, D.; Ye, S.; Hintennach, A.; Lu, J.; Fowler, M.; Chen, Z. *Nat. Energy* **2018**, *3*, 279–289.
- (6) Crabtree, G. *Science* **2019**, *366*, 422–424.

- (7) Tian, Y.; Zeng, G.; Rutt, A.; Shi, T.; Kim, H.; Wang, J.; Koettgen, J.; Sun, Y.; Ouyang, B.; Chen, T.; Lun, Z.; Rong, Z.; Persson, K.; Ceder, G. *Chem. Rev.* **2020**, *121*, 1623–1669.
- (8) Whittingham, M. S. *Chem. Rev.* **2014**, *114*, 11414–11443.
- (9) Muldoon, J.; Bucur, C. B.; Gregory, T. *Chem. Rev.* **2014**, *114*, 11683–11720.
- (10) Canepa, P.; Gautam, G. S.; Hannah, D. C.; Malik, R.; Liu, M.; Gallagher, K. G.; Persson, K. A.; Ceder, G. *Chem. Rev.* **2017**, *117*, 4287–4341.
- (11) de Dompablo, M. E. A.; Ponrouch, A.; Johansson, P.; Palacín, M. R. *Chem. Rev.* **2019**, *120*, 6331–6357.
- (12) Kharbachi, A. E.; Zavorotynska, O.; Latroche, M.; Cuevas, F.; Yartys, V.; Fichtner, M. *J. Alloys Compd.* **2020**, *817*, 153261.
- (13) Blanc, L. E.; Kundu, D.; Nazar, L. F. *Joule* **2020**, *4*, 771–799.
- (14) Peled, E.; Meitav, A.; Brand, M. *J. Electrochem Soc.* **1981**, *128*, 1936–1938.
- (15) Aurbach, D.; Skaletsky, R.; Gofer, Y. *J. Electrochem. Soc.* **1991**, *138*, 3536–3545.
- (16) See, K. A.; Gerbec, J. A.; Jun, Y.-S.; Wudl, F.; Stucky, G. D.; Seshadri, R. *Adv. Energy Mater.* **2013**, *3*, 1056–1061.
- (17) Ponrouch, A.; Frontera, C.; Bardé, F.; Palacín, M. R. *Nat. Mater.* **2015**, *15*, 169–172.
- (18) Wang, D.; Gao, X.; Chen, Y.; Jin, L.; Kuss, C.; Bruce, P. G. *Nat. Mater.* **2017**, *17*, 16–20.
- (19) Hahn, N. T.; Seguin, T. J.; Lau, K.-C.; Liao, C.; Ingram, B. J.; Persson, K. A.; Zavadil, K. R. *J. Am. Chem. Soc.* **2018**, *140*, 11076–11084.

- (20) Li, Z.; Fuhr, O.; Fichtner, M.; Zhao-Karger, Z. *Energy & Environmental Science* **2019**, *12*, 3496–3501.
- (21) Shyamsunder, A.; Blanc, L. E.; Assoud, A.; Nazar, L. F. *ACS Energy Letters* **2019**, *4*, 2271–2276.
- (22) Scafuri, A.; Berthelot, R.; Pirnat, K.; Vizintin, A.; Bitenc, J.; Aquilanti, G.; Foix, D.; Dedryvère, R.; Arçon, I.; Dominko, R.; Stievano, L. *Chem. Mater.* **2020**, *32*, 8266–8275.
- (23) Bitenc, J.; Scafuri, A.; Pirnat, K.; Lozinšek, M.; Jerman, I.; Grdadolnik, J.; Fraisse, B.; Berthelot, R.; Stievano, L.; Dominko, R. *Batteries Supercaps* **2020**, *4*, 214–220.
- (24) Yang, F.; Liu, Y.-S.; Feng, X.; Qian, K.; Kao, L. C.; Ha, Y.; Hahn, N. T.; Seguin, T. J.; Tsige, M.; Yang, W.; Zavadil, K. R.; Persson, K. A.; Guo, J. *RSC Adv.* **2020**, *10*, 27315–27321.
- (25) Gao, X.; Liu, X.; Mariani, A.; Elia, G. A.; Lechner, M.; Streb, C.; Passerini, S. *Energy & Environmental Science* **2020**, *13*, 2559–2569.
- (26) Liang, Y.; Dong, H.; Aurbach, D.; Yao, Y. *Nature Energy* **2020**, *5*, 646–656.
- (27) Forero-Saboya, J.; Davoisne, C.; Dedryvère, R.; Yousef, I.; Canepa, P.; Ponrouch, A. *Energy Environ. Sci.* **2020**, *13*, 3423–3431.
- (28) Hahn, N. T.; Driscoll, D. M.; Yu, Z.; Sterbinsky, G. E.; Cheng, L.; Balasubramanian, M.; Zavadil, K. R. *ACS Applied Energy Materials* **2020**, *3*, 8437–8447.
- (29) Hahn, N. T.; Self, J.; Seguin, T. J.; Driscoll, D. M.; Rodriguez, M. A.; Balasubramanian, M.; Persson, K. A.; Zavadil, K. R. *J. Mater. Chem. A* **2020**, *8*, 7235–7244.
- (30) Li, Z.; Vinayan, B. P.; Diemant, T.; Behm, R. J.; Fichtner, M.; Zhao-Karger, Z. *Small* **2020**, *16*, 2001806.

- (31) Xu, Z.-L.; Park, J.; Wang, J.; Moon, H.; Yoon, G.; Lim, J.; Ko, Y.-J.; Cho, S.-P.; Lee, S.-Y.; Kang, K. *Nat. Commun.* **2021**, *12*, 3369.
- (32) Rong, Z.; Malik, R.; Canepa, P.; Gautam, G. S.; Liu, M.; Jain, A.; Persson, K.; Ceder, G. *Chem. Mater.* **2015**, *27*, 6016–6021.
- (33) Chen, T.; Gautam, G. S.; Canepa, P. *Chem. Mater.* **2019**, *31*, 8087–8099.
- (34) Bölle, F. T.; Mathiesen, N. R.; Nielsen, A. J.; Vegge, T.; Garcia-Lastra, J. M.; Castelli, I. E. *Batteries & Supercaps* **2020**, *3*, 488–498.
- (35) Canepa, P.; Bo, S.-H.; Gautam, G. S.; Key, B.; Richards, W. D.; Shi, T.; Tian, Y.; Wang, Y.; Li, J.; Ceder, G. *Nat. Commun.* **2017**, *8*, 1759.
- (36) Kim, S.; Yin, L.; Lee, M. H.; Parajuli, P.; Blanc, L.; Fister, T. T.; Park, H.; Kwon, B. J.; Ingram, B. J.; Zapol, P.; Klie, R. F.; Kang, K.; Nazar, L. F.; Lapidus, S. H.; Vaughey, J. T. *ACS Energy Lett.* **2020**, *5*, 3203–3211.
- (37) Gautam, G. S.; Canepa, P.; Malik, R.; Liu, M.; Persson, K.; Ceder, G. *Chem. Commun.* **2015**, *51*, 13619–13622.
- (38) Amatucci, G. G.; Badway, F.; Singhal, A.; Beaudoin, B.; Skandan, G.; Bowmer, T.; Plitz, I.; Pereira, N.; Chapman, T.; Jaworski, R. *J Electrochem Soc* **2001**, *148*, A940.
- (39) Verrelli, R.; Black, A.; Pattanathummasid, C.; Tchitchekova, D.; Ponrouch, A.; Oró-Solé, J.; Frontera, C.; Bardé, F.; Rozier, P.; Palacín, M. *J. Power Sources* **2018**, *407*, 162–172.
- (40) Murata, Y.; Takada, S.; Obata, T.; Tojo, T.; Inada, R.; Sakurai, Y. *Electrochim. Acta* **2019**, *294*, 210–216.
- (41) Tchitchekova, D. S.; Ponrouch, A.; Verrelli, R.; Broux, T.; Frontera, C.; Sorrentino, A.; Bardé, F.; Biskup, N.; de Dompablo, M. E. A.; Palacín, M. R. *Chem. Mater.* **2018**, *30*, 847–856.

- (42) Verrelli, R.; Black, A.; Dugas, R.; Tchitchekova, D.; Ponrouch, A.; Palacin, M. R. *J. Electrochem. Soc.* **2020**, *167*, 070532.
- (43) Verrelli, R.; Black, A. P.; Frontera, C.; Oró-Solé, J.; de Dompablo, M. E. A.; Fuertes, A.; Palacín, M. R. *ACS Omega* **2019**, *4*, 8943–8952.
- (44) Cabello, M.; Nacimiento, F.; Alcántara, R.; Lavela, P.; Vicente, C. P.; Tirado, J. L. *Chem. Mater.* **2018**, *30*, 5853–5861.
- (45) Hohenberg, P.; Kohn, W. *Phys. Rev.* **1964**, *136*, B864–B871.
- (46) Kohn, W.; Sham, L. J. *Phys. Rev.* **1965**, *140*, A1133–A1138.
- (47) de Dompablo, M. E. A.; Krich, C.; Nava-Avendaño, J.; Biškup, N.; Palacín, M. R.; Bardé, F. *Chem. Mater.* **2016**, *28*, 6886–6893.
- (48) de Dompablo, M. E. A.; Krich, C.; Nava-Avendaño, J.; Palacín, M. R.; Bardé, F. *Phys. Chem. Chem. Phys.* **2016**, *18*, 19966–19972.
- (49) Torres, A.; Luque, F.; Tortajada, J.; de Dompablo, M. A. *Energy Storage Mater.* **2019**, *21*, 354–360.
- (50) Torres, A.; Casals, J. L.; de Dompablo, M. E. A. *Chem. Mater.* **2021**, *33*, 2488–2497.
- (51) Torres, A.; Bardé, F.; de Dompablo, M. A. *Solid State Ionics* **2019**, *340*, 115004.
- (52) Black, A. P.; Torres, A.; Frontera, C.; Palacín, M. R.; de Dompablo, M. E. A. *Dalton Trans.* **2020**, *49*, 2671–2679.
- (53) Rogosic, J. PhD Thesis: Towards the development of calcium ion batteries. Ph.D. thesis, Massachusetts Institute of Technology. Department of Materials Science and Engineering., 2014; Pages 1–190.
- (54) Bergerhoff, G.; Hundt, R.; Sievers, R.; Brown, I. D. *J. Chem. Inf. Comput. Sci.* **1983**, *23*, 66–69.

- (55) Hellenbrandt, M. *Crystallogr. Rev.* **2004**, *10*, 17–22.
- (56) Brown, I. D. *Acta Crystallogr.* **1988**, *44*, 545–553.
- (57) Yang, L.; Dacek, S.; Ceder, G. *Phys. Rev. B* **2014**, *90*, 054102.
- (58) Jain, A.; Ong, S. P.; Hautier, G.; Chen, W.; Richards, W. D.; Dacek, S.; Cholia, S.; Gunter, D.; Skinner, D.; Ceder, G.; Persson, K. A. *APL Mater.* **2013**, *1*, 011002.
- (59) Sun, W.; Dacek, S. T.; Ong, S. P.; Hautier, G.; Jain, A.; Richards, W. D.; Gamst, A. C.; Persson, K. A.; Ceder, G. *Sci. Adv.* **2016**, *2*, e1600225.
- (60) Hannah, D. C.; Gautam, G. S.; Canepa, P.; Ceder, G. *Adv. Energy Mater.* **2018**, *8*, 1800379.
- (61) Levi, E.; Gofer, Y.; Vestfried, Y.; Lancry, E.; Aurbach, D. *Chem. Mater.* **2002**, *14*, 2767–2773.
- (62) Levi, M. D.; Lancry, E.; Levi, E.; Gizbar, H.; Gofer, Y.; Aurbach, D. *Solid State Ionics* **2005**, *176*, 1695–1699.
- (63) Levi, E.; Aurbach, D. *Chem. Mater.* **2010**, *22*, 3678–3692.
- (64) Smeu, M.; Hossain, M. S.; Wang, Z.; Timoshevskii, V.; Bevan, K. H.; Zaghbi, K. *Journal of Power Sources* **2016**, *306*, 431–436.
- (65) Juran, T. R.; Smeu, M. *Phys. Chem. Chem. Phys.* **2017**, *19*, 20684–20690.
- (66) Handbook, C. *CRC Handbook of Chemistry and Physics, 88th Edition*, 88th ed.; CRC Press, 2007.
- (67) Carrasco, J. *J. Phys. Chem. C* **2014**, *118*, 19599–19607.
- (68) Das, T.; Tosoni, S.; Pacchioni, G. *Comput. Mater. Sci.* **2021**, *191*, 110324.

- (69) Tchitchekova, D. S.; Frontera, C.; Ponrouch, A.; Krich, C.; Bardé, F.; Palacín, M. R. *Dalton Trans.* **2018**, *47*, 11298–11302.
- (70) Hannah, D. C.; Gautam, G. S.; Canepa, P.; Rong, Z.; Ceder, G. *Chemical Communications* **2017**, *53*, 5171–5174.
- (71) Koettgen, J.; Bartel, C. J.; Shen, J.-X.; Persson, K. A.; Ceder, G. *Phys. Chem. Chem. Phys.* **2020**, *22*, 27600–27604.
- (72) Zhang, Z.; Zhang, X.; Zhao, X.; Yao, S.; Chen, A.; Zhou, Z. *ACS Omega* **2019**, *4*, 7822–7828.
- (73) Henkelman, G.; Jónsson, H. *J. Chem. Phys.* **2000**, *113*, 9978–9985.
- (74) Martinolich, A. J.; Lee, C.-W.; Lu, I.-T.; Bevilacqua, S. C.; Preefer, M. B.; Bernardi, M.; Schleife, A.; See, K. A. *Chem. Mater.* **2019**, *31*, 3652–3661.
- (75) Shannon, R. D. *Acta Crystallogr A* **1976**, *32*, 751–767.
- (76) Gautam, G. S.; Sun, X.; Duffort, V.; Nazar, L. F.; Ceder, G. *J. Mater. Chem. A* **2016**, *4*, 17643–17648.
- (77) Henkelman, G.; Uberuaga, B. P.; Jónsson, H. *J. Chem. Phys.* **2000**, *113*, 9901–9904.
- (78) Perdew, J. P.; Burke, K.; Ernzerhof, M. *Phys. Rev. Lett.* **1996**, *77*, 3865–3868.
- (79) Kresse, G.; Furthmüller, J. *Phys. Rev. B* **1996**, *54*, 11169–11186.
- (80) Kresse, G.; Furthmüller, J. *Computational Materials Science* **1996**, *6*, 15–50, 32372.
- (81) Kresse, G.; Joubert, D. *Phys. Rev. B* **1999**, *59*, 1758–1775.
- (82) Wang, L.; Maxisch, T.; Ceder, G. *Phys. Rev. B* **2006**, *73*, 195107.
- (83) Zhou, F.; Maxisch, T.; Ceder, G. *Phys. Rev. Lett.* **2006**, *97*, 155704.

- (84) Franchini, C.; Podloucky, R.; Paier, J.; Marsman, M.; Kresse, G. *Phys. Rev. B* **2007**, *75*, 195128.
- (85) Hinuma, Y.; Meng, Y. S.; Ceder, G. *Phys. Rev. B* **2008**, *77*.
- (86) Jain, A.; Hautier, G.; Ong, S. P.; Moore, C. J.; Fischer, C. C.; Persson, K. A.; Ceder, G. *Phys. Rev. B* **2011**, *84*.
- (87) Sai Gautam, G.; Carter, E. A. *Phys. Rev. Materials* **2018**, *2*, 095401.
- (88) Dudarev, S. L.; Botton, G. A.; Savrasov, S. Y.; Humphreys, C. J.; Sutton, A. P. *Phys. Rev. B* **1998**, *57*, 1505–1509.
- (89) Sheppard, D.; Terrell, R.; Henkelman, G. *The Journal of Chemical Physics* **2008**, *128*, 134106.

Graphical TOC Entry

